Intruder in a two-dimensional granular system: Effects of dynamic and static basal friction on stick-slip and clogging dynamics

C. Manuel Carlevaro [1,*] Ryan Kozlowski [2] Luis A. Pugnaloni [3] Hu Zheng [2,4]
Joshua E. S. Socolar [2] and Lou Kondic [5]

[1]*Instituto de Física de Líquidos y Sistemas Biológicos, CONICET, 59 789, 1900 La Plata, Argentina*
and Departamento de Ingeniería Mecánica, Universidad Tecnológica Nacional, Facultad Regional La Plata, La Plata, 1900, Argentina
[2]*Department of Physics, Duke University, Durham, North Carolina 27708, USA*
[3]*Departamento de Física, Facultad Ciencias Exactas y Naturales, Universidad Nacional de La Pampa, CONICET,
Uruguay 151, 6300 Santa Rosa (La Pampa), Argentina*
[4]*Department of Geotechnical Engineering, College of Civil Engineering, Tongji University, Shanghai, 200092, China*
[5]*Department of Mathematical Sciences and Center for Applied Mathematics and Statistics, New Jersey Institute of Technology,
Newark, New Jersey 07102, USA*

We present simulation results for an intruder pulled through a two-dimensional granular system by a spring using a model designed to mimic the experiments described by Kozlowski *et al.* [Phys. Rev. E **100**, 032905 (2019)]. In that previous study the presence of basal friction between the grains and the base was observed to change the intruder dynamics from clogging to stick-slip. Here we first show that our simulation results are in excellent agreement with the experimental data for a variety of experimentally accessible friction coefficients governing interactions of particles with each other and with boundaries. We then use simulations to explore a broader range of parameter space, focusing on the friction between the particles and the base. We consider both static and dynamic basal friction coefficients, which are difficult to vary smoothly in experiments. The simulations show that dynamic friction strongly affects the stick-slip behavior when the coefficient is decreased below 0.1, while static friction plays only a marginal role.

I. INTRODUCTION

Granular media respond in a variety of ways to applied loads, such as boundary shear [1–3], intruding rods [4,5], or surface sliders [3,6,7], exhibiting behaviors that include fluidlike flow, solidlike rigidity, and (sometimes periodic) cycles of stability and failure [8]. The response of a granular medium to a point-load, or single-grain perturbation, is a particularly sensitive probe of the connection between grain-scale dynamics and large-scale material stability and failure. Recent granular point-load studies have focused on the dynamical response of a single-grain intruder, mostly in quasi-two-dimensional (2D) beds of disks [9–14]. In all cases, the dynamics is affected by the packing fraction and the strength of the driving mechanism, whether the intruder is driven at a constant velocity, by a constant force, or by a continually loading spring. An experiment on intruder dynamics in a 2D Couette geometry showed that friction between the particles and the supporting substrate (basal friction) also has a strong effect [15], as had previously been observed only in the context of quasistatic shear-jamming [16].

The key findings of the quasi-2D Couette experiment of Ref. [15] was that there are two nontrivial, qualitatively distinct regimes of intruder dynamics, and the crossover between them is controlled by frictional interactions with the substrate as well as by packing fraction. For high packing fractions and a typical friction coefficient, the intruder advances through a sequence of rapid slip events separated by extended periods of very slow creep during which the external force on the intruder is slowly increased. For lower packing fractions, or in the absence of basal friction, the intruder motion consists of long periods with average speed equal to the drive speed, punctuated by occasional clogging events. (For still smaller packing fractions, the intruder carves out an open channel and moves freely through it.) The experiments yield statistics of the intruder velocity, of the forces applied by the driver, and of the waiting times between sticking periods, which all show a crossover between the stick-slip and intermittent flow regimes.

In the present work, we develop a numerical model of an intruder dragged through a 2D granular layer, which effectively models the system studied experimentally in Ref. [15]. We then report on model simulations with friction parameters not easily accessible in experiments. By smoothly varying the basal dynamic and static friction coefficients from zero to the experimental value, we show that the dynamic friction coefficient μ_d^{pb} controls the overall dynamics, with $\mu_d^{\mathrm{pb}} > 0.1$ leading to clear stick-slip behavior and smaller μ_d^{pb} leading to intermittent flow. The static friction coefficient, μ_s^{pb}, on the other hand, plays only a marginal role in determining the intruder's dynamical behavior. It thus appears that the qualitative behavior is determined by the dynamical processes

---

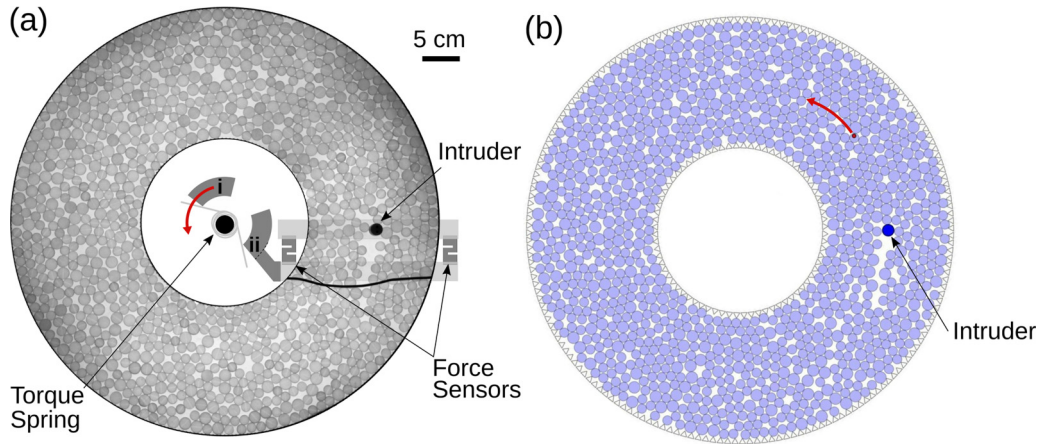*Corresponding author: manuel@iflysib.unlp.edu.ar

FIG. 1. (a) Top-down schematic of the experiment with a sample image of grains. One end of the torque spring (i) is driven at a constant angular velocity (direction indicated by curved arrow) by a stepper motor. The other end of the torque spring (ii) is rigidly fixed to the pusher arm that holds the intruder in the static 2D layer of polyurethane photoelastic disks. (b) Snapshot of a sample simulation. The red dot indicates the position of the end of the torque spring that is being driven at constant angular velocity (direction indicated by curved arrow); the other end of the spring is attached to the dark blue particle, which is the intruder. The light blue particles are the bidisperse grains, and the static inner and outer boundaries are formed by equilateral triangles. A movie of the dynamics is available in the Supplemental Material [17].

that select the sampled configurations, rather than the static friction that helps stabilize stationary (jammed) states.

The paper is organized as follows. In Sec. II, we briefly review the experimental setup and then describe the simulation procedure. Section III contains our key results. After describing the two dynamical regimes of intruder motion, we compare the experimental and simulation results for different packing fractions for both frictional and frictionless substrates. We then present simulation results for a range of static and dynamic basal friction coefficients. Section IV contains our conclusions and some remarks on questions of further interest.

II. MODEL SYSTEM

Figure 1(a) shows the experimental system that we attempt to model. A bidisperse layer of ∼1000 plastic disks is confined to an annular region by fixed boundaries lined with ribbed rubber. An intruder disk is pushed in the azimuthal direction by means of an arm attached to a torque spring that is loaded at a constant rate. The particles either sit on a glass base and experience frictional forces (basal friction) or float on a layer of fluid that eliminates the basal friction. The intruder itself is not in contact with the base. The setup is described in detail in Ref. [15].

Our model takes the grains to be rigid disks that experience both normal and frictional forces when they are in contact with each other or the walls, as well as frictional forces with the substrate. The model is two dimensional; we do not allow buckling out of the plane, and we assume the interparticle forces have no out-of-plane component. Key parameters are chosen to match experimental values, including particle diameters and masses, dimensions of the confining annular region, driving velocity, and torque spring constant. We neglect the hydrodynamic effects of the fluid used for the frictionless base in the experiments and simply set the basal friction to zero in such cases. Despite our approximations, the statistics

of the intruder dynamics from simulations closely match the experimental results when the experimental values for the particle-particle and particle-base static and dynamic friction are used.

We have carried out discrete element method (DEM) simulations of the model using the Box2D library [18]; a snapshot of a typical simulation is shown in Fig. 1(b). The Box2D library uses a constraint solver to handle rigid bodies. Before each time step, a series of iterations (typically 100) is used to resolve constraints on overlaps and on static friction between bodies through a Lagrange multiplier scheme [19,20]. After resolving overlaps, the inelastic collision at each contact is solved and new linear and angular velocities are assigned to each body. The equations of motion are integrated through a symplectic Euler algorithm. Solid friction between grains is also handled by means of a Lagrange multiplier scheme that implements the Coulomb criterion with the dynamic and static friction coefficients set to be equal. The approach yields realistic dynamics for granular bodies with complex shapes [19], including sharp corners, and has been successfully used to study grains under tapping protocols [21,22] and under vigorous vibration [23].

A. Cell

The cell consists of two immobile concentric boundary "rings" forming an annular 2D Couette cell. The boundaries are formed by small equilateral triangles facing inward (toward the annular channel), which prevent particles from slipping at the boundary, serving the role of the ribbed rubber in the experiments. The inner ring consists of 72 triangles of side length $0.682d$, where d is the diameter of the small particles used for the granular pack (see Sec. II B); the outer ring consists of 180 triangles of side length $0.683d$. The inner and outer rings are $8.810d$ and $22.800d$ in radius.

Gravity (with acceleration g) acts in the direction perpendicular to the Couette plane. The base on which the circular

TABLE I. List of packing fractions explored in the simulations and the corresponding numbers of large and small particles.

ϕ	N_l	N_s
0.6480	245	676
0.6589	250	685
0.6691	253	697
0.6797	257	708
0.6899	260	720
0.6998	264	730
0.7104	268	741
0.7203	272	751
0.7308	276	762
0.7414	280	773
0.7513	284	783
0.7619	288	794
0.7724	292	805
0.7824	296	815

particles rest is modeled by implementing an effective solid friction as follows. If a particle is moving at a speed above a small threshold v' (i.e., $|\boldsymbol{v}| > v'$), then a dynamic friction force with the base $F_d^{\mathrm{pb}} = -\mu_d^{\mathrm{pb}} mg\boldsymbol{v}/|\boldsymbol{v}|$ is applied to the center of mass of the particle. Whenever $|\boldsymbol{v}| < v'$, the particle is immobilized by setting $\boldsymbol{v} = 0$. If at rest, then the particle will only resume translational motion if the total external force exerted by other particles exceeds the static friction force with the base set to $F_s^{\mathrm{pb}} = \mu_s^{\mathrm{pb}} mg$, with $\mu_s^{\mathrm{pb}} = v'/(g\,dt)$, where dt is the simulation time step. This ensures that a particle will resume motion only if its initial velocity due to the collisions in the previous time step exceeds the velocity threshold v'. In the present work, we hold dt fixed, so the static friction coefficient is controlled via v'. We do not implement rotational friction forces between the particles and the base in this model.

B. Disks

The annulus is filled with a large to small $1:2.75$ bidisperse mixture of circular particles of same material density. The small particles have diameter d and mass m. The larger particles have diameter $d_l = 1.25d$ and $m_l = (d_l/d)^2 m = 1.5625m$. The packing fraction is set by inserting a given number of disks ($N = N_s + N_l$, where N_s and N_l are the number of small and large particles, respectively), conserving the $1:2.75$ number ratio. Table I lists all packing fractions explored. For the calculation of the packing fraction we exclude both the area of the triangles and the space between them.

Each disk interacts with other disks, the boundaries of the cell, and the intruder disk (see Sec. II C) as a perfectly rigid impenetrable object. The result of a collision is controlled by a restitution coefficient ϵ and the static μ_s and dynamic μ_d friction coefficients. Unless explicitly noted, we take $\mu_s = \mu_d$. Note that the particle-base interaction has $\mu_s^{\mathrm{pb}} \neq \mu_d^{\mathrm{pb}}$ (see Sec II A). Table II lists the parameters for the various pairwise interactions in the system. To reduce computational costs, we set ϵ to a low value, which reduces the number of collisions per unit time that must be resolved. We have observed that this choice does not affect the agreement obtained with the experimental results.

TABLE II. List of friction and restitution coefficients for the various pairwise interactions in the system. The numerical values for the friction parameters are motivated by the ones measured in the experiments.

	Acronym	μ_s	μ_d	ϵ
Particle-particle	pp	1.20	1.20	0.05
Particle-annulus	pa	0.77	0.77	0.05
Particle-intruder	pi	0.41	0.41	0.05
Particle-base	pb	[0.36;1.00]	[0;0.36]	—
Intruder-base	ib	0.00	0.00	—

C. Intruder

A circular particle of diameter $1.25d$ (the size of a large particle) is used as an intruder. The intruder interacts only with the other disks, not with the base (see Table II) as in the experiments, where the intruder is suspended above the base at all times.

The intruder is constrained to move along a circle of radius $15.8d$ centered at the annulus center. This is done by binding the intruder to a very stiff radial spring. A "soft" torque spring ($K = 3591.98mgd/\mathrm{rad}$) is connected to the intruder and rotated counterclockwise at a low constant angular speed, $\omega = 0.00432\sqrt{g/d}$. This drives the intruder through the pack of disks. The attached spring can only pull the intruder; if the spring becomes shorter than its equilibrium length, no force is applied. The mass of the intruder is set to $380m$, a mass that yields the same moment of inertia with respect to the center of the annulus as the relevant moment of inertia in the experiment, which includes both the pushing arm and the intruder. The simulation time step is $0.001\sqrt{d/g}$ and the instantaneous intruder position and velocity (and spring force) are recorded every 100 time steps. The time step is sufficiently small to avoid numerical instabilities; the results are consistent for smaller time steps.

III. RESULTS

For each simulation run, the intruder is driven completely around the annulus at least twice and at most 10 times (as was done in the experiments). For all statistical analyses, we ignore the first revolution, in which transient effects are observed as the intruder moves through an initially random configuration of grains. The friction coefficients and packing fractions of the experiments, as well as the postprocessing performed on intruder velocity and force data, are matched in simulation. We first validate simulations by comparing the statistics of intruder velocity, spring force, creep velocity during sticking periods, and waiting times between sticking periods with those of the experiment. We then vary the static and dynamic basal friction coefficients to elucidate their roles in determining the intruder dynamics.

A. Stick-slip dynamics

Figure 2 shows examples of time series for the intruder velocity and force, where time is measured in terms of the cumulative drive angle $\theta = \omega t$. The force measured in experiments is the force of the grains acting on the intruder
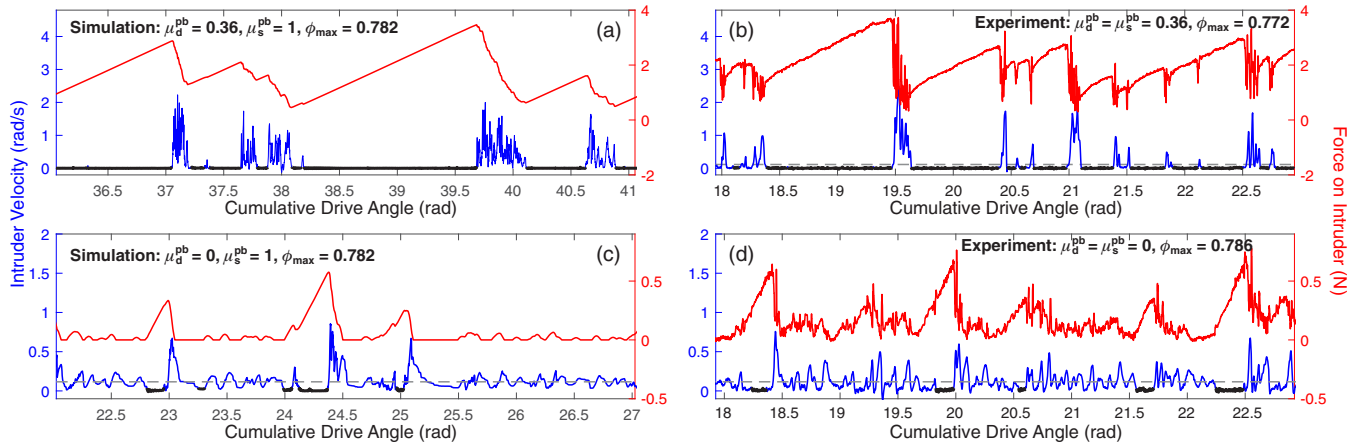
FIG. 2. Sample time series at maximum packing fraction for cases with basal friction [(a) and (b)] and without [(c) and (d)] in both simulation [(a) and (c)] and experiment [(b) and (d)]. Thick black overlay plots indicate detected sticking periods.

[compression of the force sensors, shown in Fig. 1(a), that hold the intruder] while in simulations the force presented is that exerted by the torque spring on the intruder. In a static configuration, these forces are the same, but while the intruder is moving, as during slips, the experimental force fluctuates more, as discussed further below. The packing fractions used for Fig. 2 are the highest packing fractions ϕ_{max} explored in both simulation and experiment (which are slightly different in the simulations for different values of the basal friction coefficient). Higher packing fractions could not be studied with the present experimental apparatus due to buckling of the particles out of plane. The thick, black overlay plots on intruder velocity are detected sticking periods, which are defined as series of consecutive data points in the intruder velocity that fall below threshold 0.04 rad/s for a duration of at least 0.4 s.

Figure 2 shows that simulations [Figs. 2(a) and 2(c)] and experiments [Figs. 2(b) and 2(d)] at comparable packing fractions produce qualitatively similar results for two different values of the basal friction coefficient. For a frictional base ($\mu_d^{pb} = 0.36$), the intruder displays a clear stick-slip dynamics, characterized by extended sticking periods followed by rapid slip events. During sticking periods the intruder velocity is nominally zero and the force of the grains (and torque spring) acting on the intruder increases approximately linearly with time. The granular medium eventually yields under the increasing point load, and a slip event occurs. During a slip, the intruder's velocity fluctuates irregularly as it collides with many grains until the medium forms a stable structure again. In the experiments, the measured force fluctuates rapidly as the load cells register numerous collisions with grains. In the simulations, the measured force is of the torque spring acting on the intruder, with fluctuations that are relatively small compared to the force itself.

For a frictionless base, both experiments and simulations show long periods of time during which the intruder moves at the drive speed with superimposed fluctuations. Occasionally, the intruder does get stuck for a short period and then slips. This behavior is reminiscent of clogging of grains that flow through a restricted aperture; we refer to it as intermittent flow dynamics [15].

B. Comparison between simulations and experiments

Figures 3 and 4 show the probability distribution functions (PDF) of the intruder velocity and the spring force in simulations and experiments. We have tested a range of packing fractions, ϕ, for the frictional and the frictionless base. The range explored for the frictionless base is narrower because in this case even at relatively high ϕ the intruder simply moves at the drive velocity, very rarely getting stuck. Figure 3 shows that the agreement between experiments and simulations is remarkably good. Note that the range of velocities observed is consistent as well as the qualitative forms of the distributions. In the frictional case, for low ϕ, the velocity distribution has its maximum at the drive speed. However, at high ϕ, this peak disappears and the maximum occurs at zero velocity, due to the fact that the intruder is stuck most of the time. These two distinct regimes are separated by a smooth transition region. Following Ref. [15], we refer to these two regimes as a stick-slip regime for high ϕ and as an intermittent flow regime at low ϕ. In the case of the frictionless base, we observe only the intermittent flow, independent of the value of ϕ.

Figure 4 shows that the spring force PDFs are very similar in experiments and simulations. The range of forces and the positions of the maxima in the experiments are very well captured by the simulations. For the frictional base, the PDFs are rather broad with a maximum at nonzero force for high ϕ. However, for low ϕ (intermittent flow) the PDF has its maximum very near zero force. Negative forces are not present in the simulations due to the modeling of the torque spring as incapable of sustaining tension. In experiments, negative forces are only measured if the spring completely decompresses and the intruder rebounds due to a collision within the central rotating axis (see Ref. [15] for more details). For the frictionless base, all ϕs lead to PDFs with a maximum at or close to zero force, consistent with the relatively free flow of the intruder. Only at very high ϕ do occasional sticking periods lead to some larger forces and therefore longer distribution tails.

Figure 5(a) shows the average force as a function of ϕ for both the frictional and the frictionless base. Overall, experimental and simulation values are very similar, with the
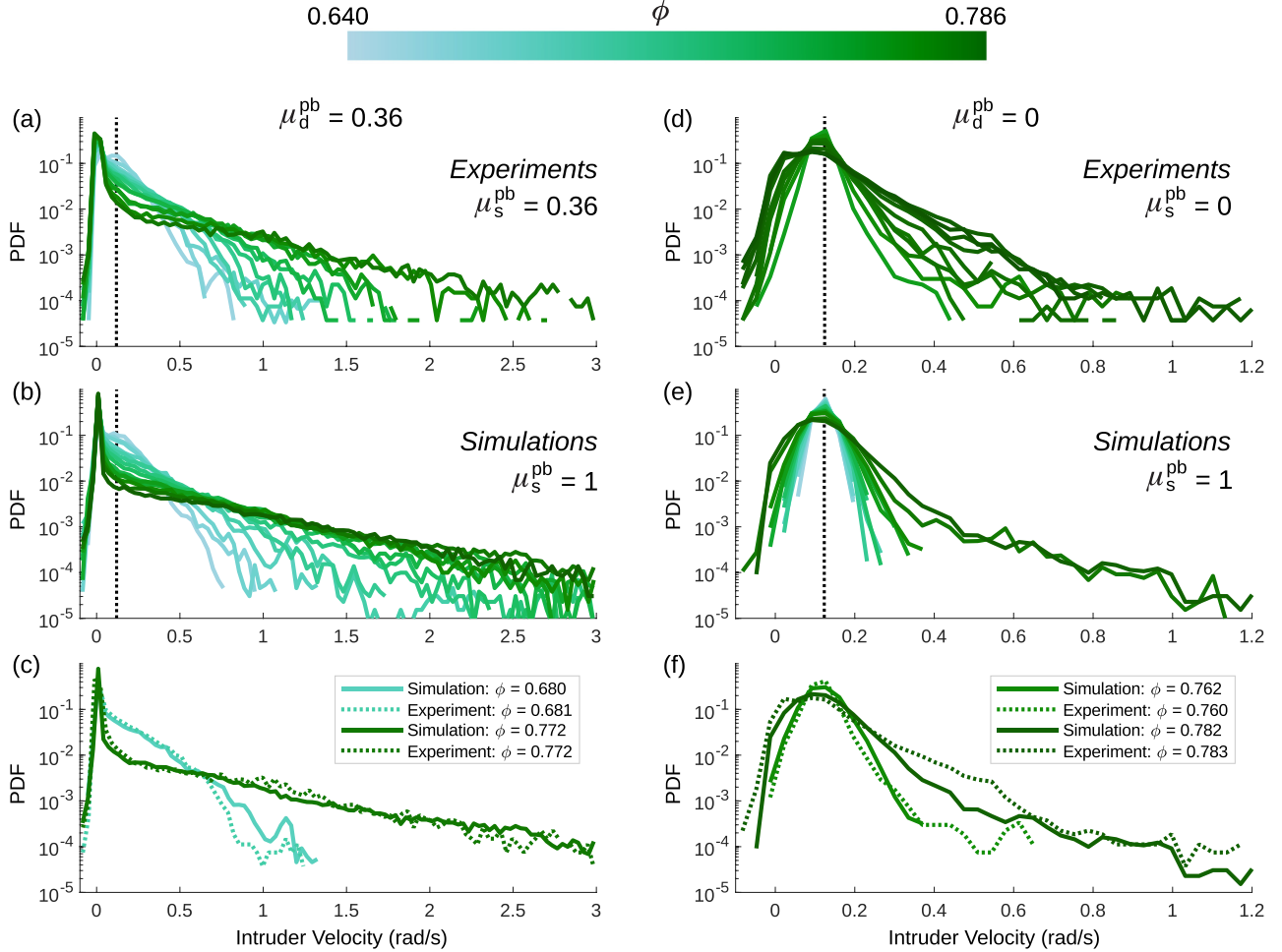
FIG. 3. Intruder velocity distribution for $\mu_d^{pb} = 0.36$ [(a)–(c)] and $\mu_d^{pb} = 0$ [(d)–(f)] bases. A range of packing fractions have been studied as indicated by the color scale. Experimental [(a) and (d)] and simulation [(b) and (e)] results show the same trends and range of velocities. Panels (c) and (f) show a direct comparison of the experimental and simulation PDF for two specific values of ϕ. The vertical dotted line in (a), (b), (d), and (e) marks the drive velocity.

exception that at high ϕ the average forces are higher in simulations, corresponding to the fact that the upper cutoffs in the distributions of Fig. 4 are somewhat larger in simulations than in experiments. As we show in Sec. III C, this quantitative difference is a consequence of running these simulations with a higher static basal friction coefficient than that measured in experiments.

We have measured two additional features of the intruder dynamics: (i) the creep velocity during sticking periods and (ii) the waiting time between consecutive sticking periods. For these statistical quantities, unless noted otherwise, we only present data from runs for which at least 20 sticking periods are detected. During a sticking period, the intruder does not remain fully static but creeps forward as the spring force increases. Figure 5(b) shows that the creep velocity is independent of ϕ when basal friction is present and is substantially larger for the frictionless base, both in simulations and experiments. Figure 5(c) shows that the average waiting time is about 10 times longer for the frictionless base than for the frictional one at the high packing fractions where sticking periods do occur in the frictionless case; sticking periods occur less frequently for $\mu_d^{pb} = 0$. With the

frictional base, for which sticking periods occur at lower ϕ, we find a mild increase of the waiting time as ϕ is decreased below 0.67. Here, too, simulations and experiments are consistent.

Given the close agreement between experiment and simulation, it appears that our simulations are a reliable tool for describing, studying, and explaining the dynamics observed in experiments. We next use simulations to explore in more detail the effect of basal friction on the intruder dynamics, which is a difficult task to carry out experimentally.

C. Effect of basal friction

As we have discussed, there is a dramatic change in the intruder dynamics when friction with the base is removed. This naturally raises the issue of whether the dynamics can be tuned continuously by changing the basal friction or whether there is a sharp transition at $\mu_d^{pb} = 0$. Controlling basal friction in the experiments is prohibitively difficult, and this is where the simulations provide novel insights.

We have run simulations with dynamic friction coefficient μ_d^{pb} in the range [0.0, 0.36] at a high packing fraction
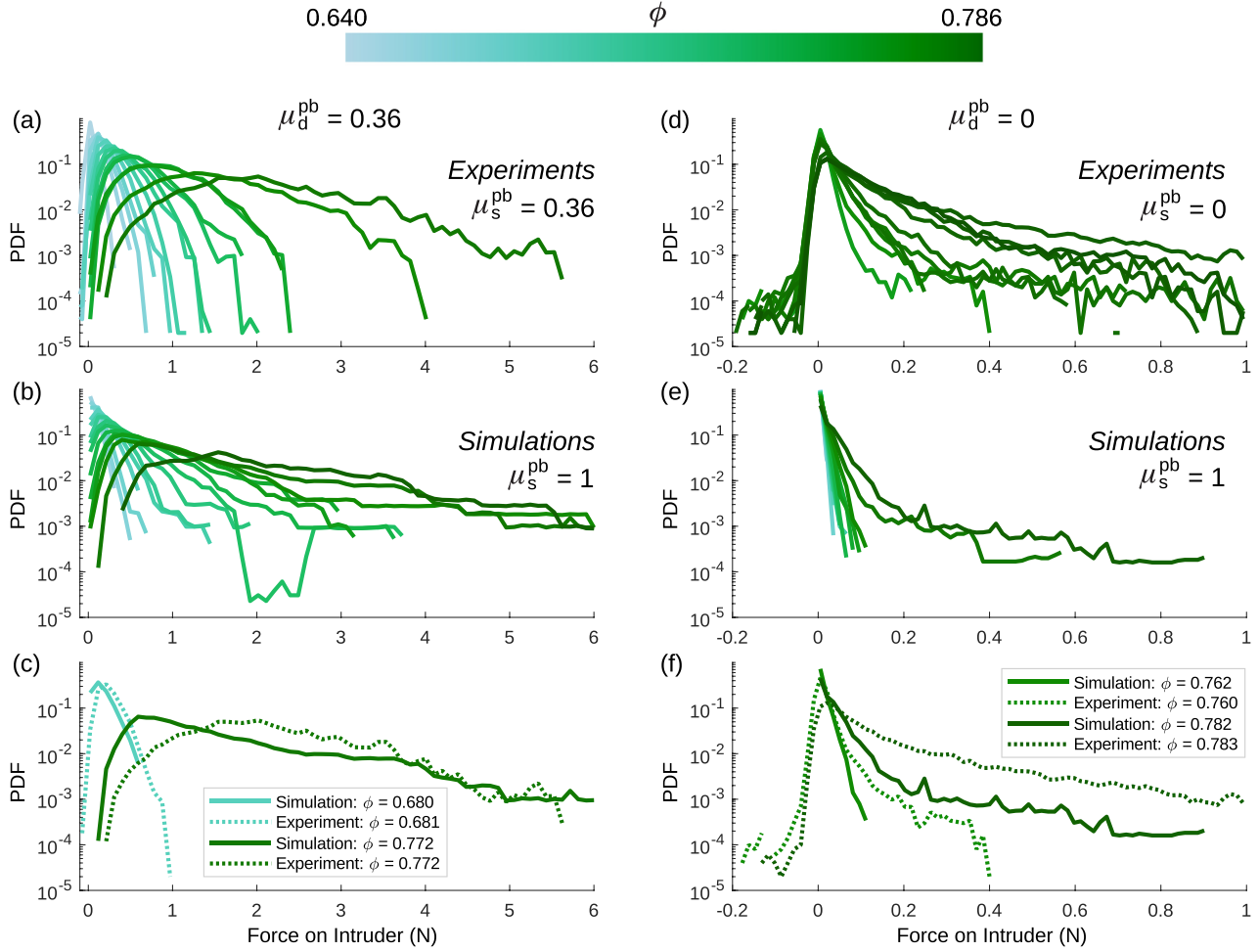
FIG. 4. Intruder force distribution for $\mu_d^{pb} = 0.36$ [(a)–(c)] and $\mu_d^{pb} = 0$ [(d)–(f)] bases. A range of packing fractions have been studied as indicated by the color scale. Experimental [(a) and (d)] and simulation [(b) and (e)] results show the same trends and range of forces. Panels (c) and (f) show a direct comparison of the experimental and simulation PDF for two specific values of ϕ.

($\phi = 0.7724$) while keeping the static friction coefficient constant at $\mu_s^{pb} = 1.0$. Figure 6 shows the intruder velocity and spring force distributions for a range of μ_d^{pb}. The spring force PDFs shown in Fig. 6(a) reveal that the probabilities for large

forces within the stick-slip regime decrease as μ_d^{pb} is decreased from 0.36 down to 0.1, indicating that the lowering of μ_d^{pb} (in the stick-slip regime) induces shorter sticking periods. Within the intermittent flow regime ($\mu_d^{pb} < 0.1$), lowering μ_d^{pb}
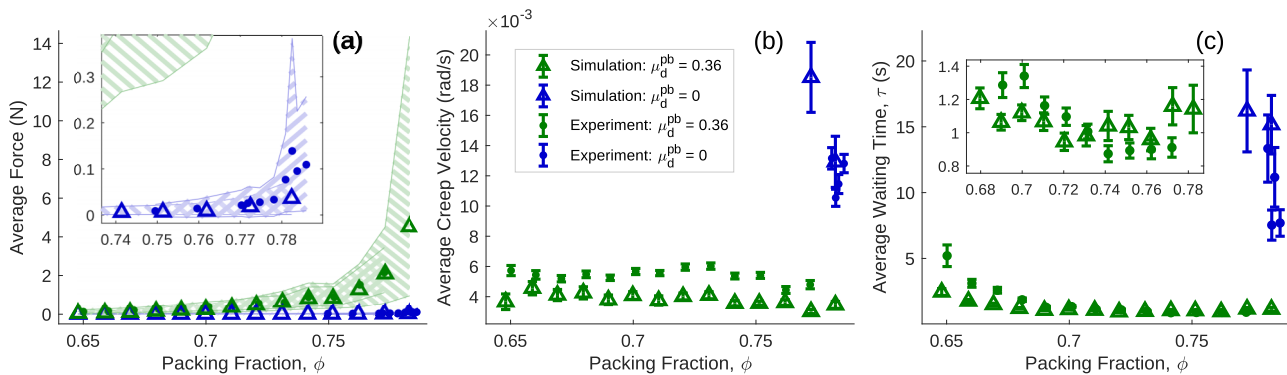

FIG. 5. (a) The average force of the force time series as a function of ϕ for the frictional (green) and the frictionless (blue) base. Open triangles correspond to simulation data and filled circles to experiments. Each shaded region ranges from the lower 10% cutoff to the upper 90% cutoff of the distribution. Error bars indicate the standard error of the average. Inset: Zoom in to highlight the case with no basal friction. (b) The average creep velocity of the intruder during detected sticking periods as a function of ϕ. (c) The average waiting time as a function of ϕ. Inset: Zoom in to highlight the case with basal friction.
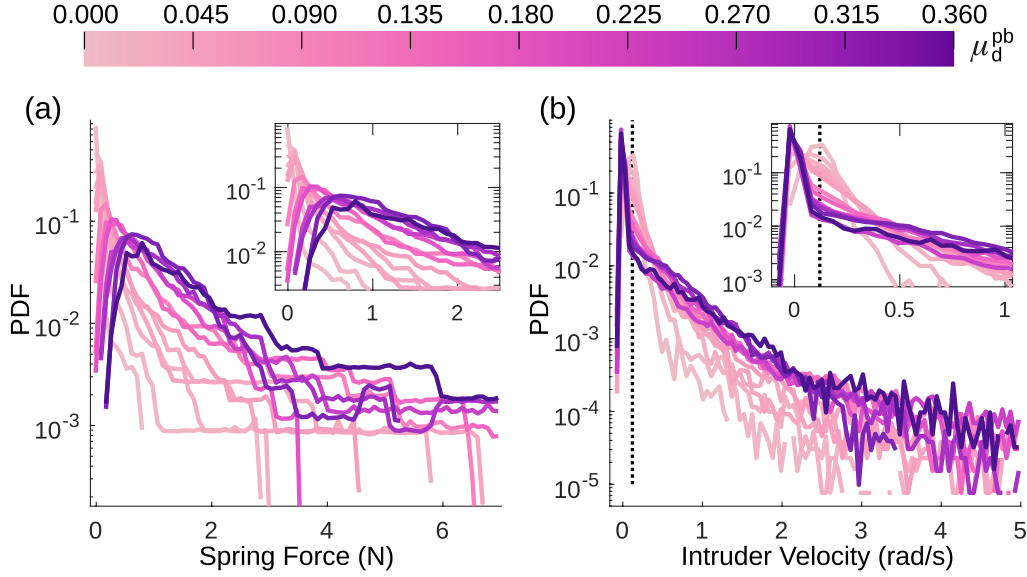
FIG. 6. PDF of the spring force (a) and the intruder velocity (b) for a range of basal dynamic friction coefficient ($0 \leqslant \mu_d^{pb} \leqslant 0.36$) and $\mu_s^{pb} = 1.0$. Insets: Zoom into the peak values of the PDFs.

leads to the appearance of a sharp peak at zero force, caused mainly by the longer periods of continuous flow between sticks. The velocity distribution shown in Fig. 6(b) seems to be nearly independent of μ_d^{pb} for $\mu_d^{pb} > 0.1$, showing a maximum at zero velocity, which is consistent with stick-slip behavior. However, for $\mu_d^{pb} < 0.1$ the maximum of the velocity PDF abruptly shifts to the spring drive speed, a characteristic of the intermittent flow regime.

Figure 7 shows the average force, average creep velocity, and average waiting time as a function of the dynamic friction coefficient μ_d^{pb}. Interestingly, the creep velocity and the average waiting time between the end of a sticking period and the beginning of the next one grow very little as the dynamic friction is decreased from 0.36 to 0.1. Thus, above $\mu_d^{pb} \approx 0.1$, a reduction in μ_d^{pb} does not significantly change the number of sticking periods (longer waiting times) and stiffness of the packing (larger creep velocities). However, a dramatic increase in both creep velocity and waiting time happens for

$\mu_d^{pb} < 0.1$, indicating a rather sharp transition between the stick-slip and intermittent flow regimes.

Figure 8 shows the average force, average creep velocity, and average waiting time for different values of basal *static* friction coefficient μ_s^{pb} for $\mu_d^{pb} = 0$ and $\mu_d^{pb} = 0.36$. In all cases we ensure $\mu_d^{pb} \leqslant \mu_s^{pb}$. Static friction seems to play a marginal role in the dynamics. The most salient feature is a marked drop in the spread of the forces [indicated by the width of the shaded region in Fig. 8(a)] for $\mu_d^{pb} = 0.36$ when μ_s^{pb} is changed from 1.0 to 0.36. This indicates that $\mu_s^{pb} > \mu_d^{pb}$ induces the occurrence of some longer lasting sticking periods, without affecting the average force significantly. This finding is confirmed in Fig. 9, which shows the PDFs for forces and intruder velocities. We note that the PDF in Fig. 9(a) for $\mu_s^{pb} = 0.36$ suggests a cutoff at large forces, in agreement with the experimental observation shown in Fig. 4. We recall here that in Fig. 4 we used $\mu_s^{pb} = 1.0$, which is somewhat above
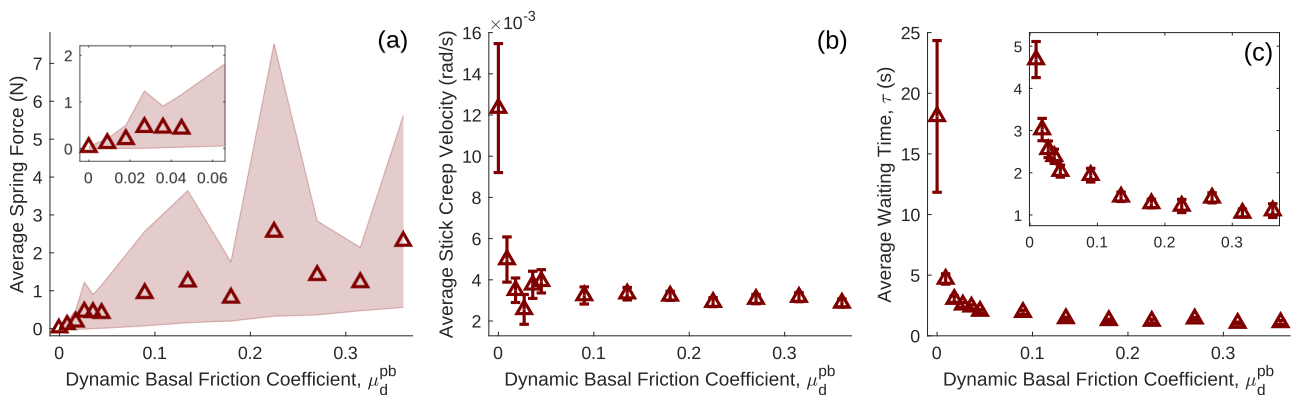

FIG. 7. Average force (a), average creep velocity during sticking periods (b), and average waiting time between sticking periods (c) as a function of μ_d^{pb} for $\mu_s^{pb} = 1.0$. Error bars indicate the standard error of the average and the shaded area indicates the 10–90% percentile in the force distribution. Note that the $\mu_d^{pb} = 0$ data point in (b) and (c) is computed from only 11 events.
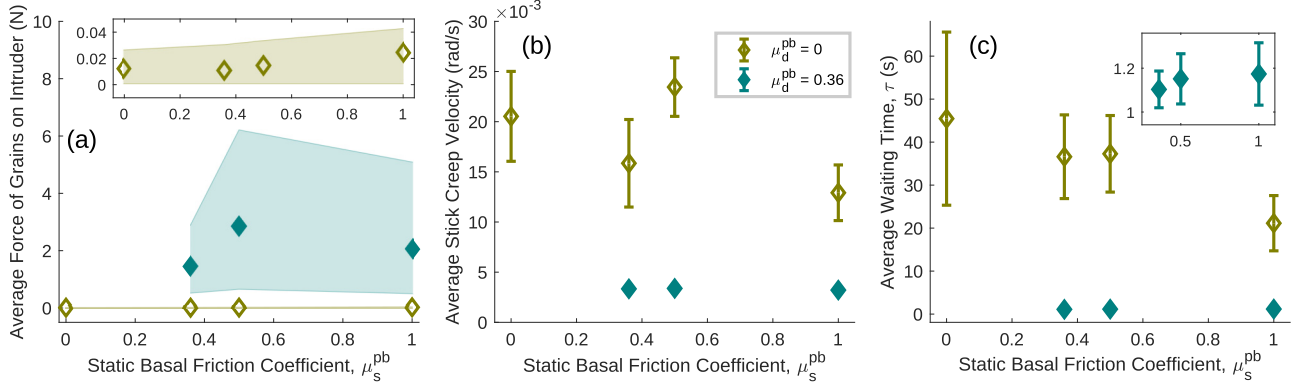
FIG. 8. Average force (a), average creep velocity during sticking periods (b), and average waiting time between sticking periods (c) as a function of the static particle-base friction μ_s^{pb} for two values of the dynamic friction: $\mu_d^{\mathrm{pb}} = 0$ (open diamonds) and $\mu_d^{\mathrm{pb}} = 0.36$ (filled diamonds). Error bars indicate the standard error of the average and the shaded area indicates the 10–90% percentile in the force distribution. Note that all of the $\mu_d^{\mathrm{pb}} = 0$ data points are computed from fewer than 20 events. For the filled diamonds, error bars are smaller than the data points.

the experimental static friction coefficient between the discs and the dry base.

IV. CONCLUSIONS

Inspired by a recent experimental finding on the dynamics of an intruder the size of a single grain dragged though a two-dimensional granular system [15], we have developed numerical simulations that allow us to deepen our understanding of the effect of basal friction. Experimentally, it has been observed that the intruder can flow rather smoothly with occasional short sticks (intermittent flow regime) or show a fully developed stick-slip dynamics. The former is observed if the base on which the particles sit is frictionless, the latter when the base is frictional. Our simulations yield results consistent with these dynamics and are also in fair quantitative agreement with the experiment.

Having validated the numerical model against the experiments, we used new simulations to investigate how the transition from intermittent flow to stick-slip is controlled by both the dynamic and the static friction coefficient of the particle-base interaction. We have shown that the transition between the two dynamic regimes (intermittent flow and stick-slip) is clearly controlled by the dynamic friction coefficient

with the base and not by the static friction coefficient. One may intuitively expect that static friction would play a major role by contributing to the stability of jammed configurations. However, one has to bear in mind that jammed configurations are reached through a dynamic process. The development of rigidity is a result of the interactions at play as particles move through unjammed configurations, making μ_d^{pb} the more relevant factor in determining the waiting times between sticking events. Our interpretation is that, for $\mu_d^{\mathrm{pb}} > 0.1$, particle motion is damped strongly enough to allow rapid formation of stable, static force network structures. Further increase in μ_d^{pb} can only marginally reduce these waiting times. Decreasing μ_d^{pb} below 0.1, however, reduces the damping enough so that particles do not quickly come to rest after a slip event is initiated. Particle-particle dissipative interactions (inelasticity and friction) then play the dominant role in slowing particles down, and this leads only to occasional clogging rather than strong sticking periods.

Static friction is expected to affect the stability of the jammed states once they occur. One of the affected features is the decay of the intruder force PDF for large forces, which is associated with the stability of the jammed states. The larger μ_s^{pb} is, the higher the probability of finding strong intruder
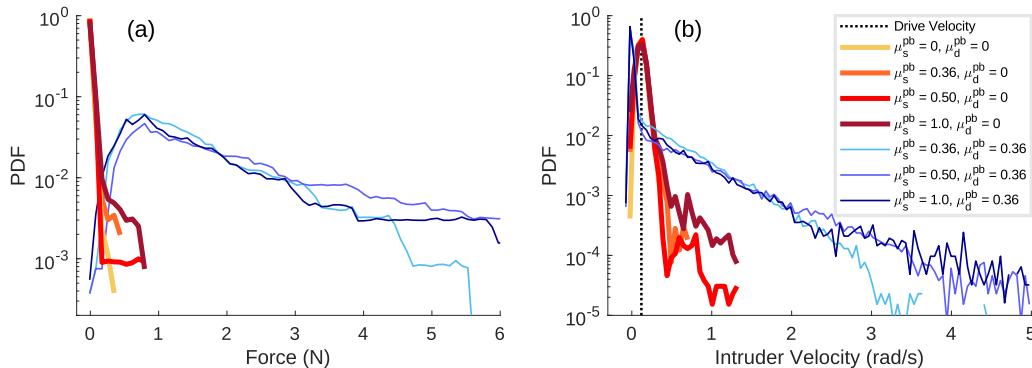

FIG. 9. PDF of the spring force (a) and the intruder velocity (b) for a range of basal static friction coefficient for two values of the dynamic friction coefficient: $\mu_d^{\mathrm{pb}} = 0$ ($0 \leqslant \mu_s^{\mathrm{pb}} \leqslant 1.0$, thick lines) and $\mu_d^{\mathrm{pb}} = 0.36$ ($0.36 \leqslant \mu_s^{\mathrm{pb}} \leqslant 1.0$, thin lines).

forces. This is indeed confirmed in Fig. 9, both for $\mu_d^{\text{pb}} = 0$ and $\mu_d^{\text{pb}} = 0.36$. Increasing μ_s^{pb} does not, however, induce a change of dynamic regime (intermittent flow or stick-slip); the main peaks in the force and velocity distributions remain unaltered. In short, static friction can only help the stick periods last longer when they do occur. The initiation of these sticking events, however, is determined solely by the basal dynamic friction.

Our results show that the additional background dissipation provided by the supporting substrate through dynamic friction is an important ingredient for stick-slip dynamics in the system studied here. It should be noted that stick-slip behavior associated with dry granular materials has been observed in the absence of a frictional substrate in other geometries [3–7]. These systems differ from ours in two potentially important ways: the driving force is applied over a length scale that is much larger than the characteristic particle size, and gravity and/or an imposed pressure over many grains creates dissipative particle-particle interactions. The latter may play a similar role to the substrate friction in our fixed volume system; in such systems, many grains are forced to be in contact such that motion within the granular medium must activate dissipative interparticle frictional forces. Moreover, studies on granular systems immersed in viscous fluids under imposed pressure (with no substrate acting on each grain) suggest that stick-slip dynamics is suppressed when particle-particle friction is decreased via lubrication [24]. Thus it appears that dissipation at the grain scale biases the system toward locally fragile or shear-jammed configurations [25]. We note that our $\mu_d^{\text{pb}} = 0$ simulation results agree qualitatively and nearly quantitatively with floating-particle experiments, suggesting that hydrodynamic effects (which were not modeled) are much less important than those associated with basal friction (or lack thereof).

Finally, it should be mentioned that simulations provide much higher resolution for velocities and forces than can be achieved in experiments. In order to compare results, we have used the same velocity threshold to detect sticking periods as was used in analyzing the experimental data. This overlooks a number of detailed features observed in the simulations during the sticking periods that may also be present in the experiments but were not resolvable in the experiments. In particular, the creep observed in simulations has a very rich structure of *microslips*. With the simulation model now validated, it will be interesting to explore the details of the dynamics that are difficult to measure in experiments, including the interparticle forces and particle displacements during microslip events.

[1] N. W. Hayman, L. Ducloué, K. L. Foco, and K. E. Daniels, Pure Appl. Geophys. **168**, 2239 (2011).

[2] J. Barés, D. Wang, D. Wang, T. Bertrand, C. S. O'Hern, and R. P. Behringer, Phys. Rev. E **96**, 052902 (2017).

[3] M. Pica Ciamarra, E. Lippiello, L. de Arcangelis, and C. Godano, Europhys. Lett. **95**, 54002 (2011).

[4] I. Albert, P. Tegzes, R. Albert, J. G. Sample, A. L. Barabási, T. Vicsek, B. Kahng, and P. Schiffer, Phys. Rev. E **64**, 031307 (2001).

[5] J.-F. Métayer, D. J. Suntrup III, C. Radin, H. L. Swinney, and M. Schröter, Europhys. Lett. **93**, 64003 (2011).

[6] S. Nasuno, A. Kudrolli, A. Bak, and J. P. Gollub, Phys. Rev. E **58**, 2161 (1998).

[7] A. Abed Zadeh, J. Barés, and R. P. Behringer, Phys. Rev. E **99**, 040901(R) (2019).

[8] H. M. Jaeger, S. R. Nagel, and R. P. Behringer, Rev. Mod. Phys. **68**, 1259 (1996).

[9] C. J. Olson Reichhardt and C. Reichhardt, Phys. Rev. E **82**, 051306 (2010).

[10] R. Candelier and O. Dauchot, Phys. Rev. E **81**, 011304 (2010).

[11] E. Kolb, P. Cixous, N. Gaudouen, and T. Darnige, Phys. Rev. E **87**, 032207 (2013).

[12] J. Geng and R. P. Behringer, Phys. Rev. E **71**, 011302 (2005).

[13] A. Seguin, C. Coulais, F. Martinez, Y. Bertho, and P. Gondret, Phys. Rev. E **93**, 012904 (2016).

[14] A. Tordesillas, J. E. Hilton, and S. T. Tobin, Phys. Rev. E **89**, 042207 (2014).

[15] R. Kozlowski, C. M. Carlevaro, K. E. Daniels, L. Kondic, L. A. Pugnaloni, J. E. S. Socolar, H. Zheng, and R. P. Behringer, Phys. Rev. E **100**, 032905 (2019).

[16] H. Zheng, J. A. Dijksman, and R. P. Behringer, Europhys. Lett. **107**, 34005 (2014).

[17] See Supplemental Material at http://link.aps.org/supplemental/10.1103/PhysRevE.101.012909 for a sample simulation video of stick-slip motion for one revolution of the intruder.

[18] Box2d physics engine, http://www.box2d.org.

[19] M. Pytlos, M. Gilbert, and C. C. Smith, Geotech. Lett. **5**, 243 (2015).

[20] E. Catto, Iterative dynamics with temporal coherence (2005), https://box2d.org/downloads/.

[21] C. Carlevaro and L. Pugnaloni, J. Stat. Mech. (2011) P01007.

[22] R. M. Irastorza, C. M. Carlevaro, and L. A. Pugnaloni, J. Stat. Mech. (2013) P12012.

[23] M. Sánchez, C. M. Carlevaro, and L. A. Pugnaloni, J. Vibr. Contr. **20**, 1846 (2014).

[24] N. Higashi and I. Sumita, J. Geophys. Res.: Solid Earth **114**, B04413 (2009).

[25] Y. Zhao, J. Barés, H. Zheng, J. E. S. Socolar, and R. P. Behringer, Phys. Rev. Lett. **123**, 158001 (2019).